The Astrophysical Journal, 852:67 (16pp), 2018 January 10 https://doi.org/10.3847/1538-4357/aa9f1f

Demarcating Circulation Regimes of Synchronously Rotating Terrestrial Planets within the Habitable Zone

Jacob Haqq-Misra[1,2], Eric. T. Wolf[3], Manoj Joshi[4,5], Xi Zhang[6], and Ravi Kumar Kopparapu[1,2,7,8]
[1] Blue Marble Space Institute of Science, 1001 4th Avenue, Suite 3201, Seattle, WA 98154, USA
[2] NASA Astrobiology Institute's Virtual Planetary Laboratory, P.O. Box 351580, Seattle, WA 98195, USA
[3] Laboratory for Atmospheric and Space Physics, Department of Atmospheric and Oceanic Sciences, University of Colorado, Boulder, Colorado, USA
[4] School of Environmental Sciences, University of East Anglia, Norwich Research Park, Norwich NR4 7TJ, UK
[5] Climatic Research Unit, University of East Anglia, Norwich Research Park, Norwich NR4 7TJ, UK
[6] Earth and Planetary Sciences Department, University of California, Santa Cruz, California, USA
[7] NASA Goddard Space Flight Center, 8800 Greenbelt Road, Mail Stop 699.0 Building 34, Greenbelt, MD 20771, USA
[8] Department of Astronomy, University of Maryland, College Park, MD 20742, USA
Received 2017 September 30; revised 2017 November 20; accepted 2017 December 1; published 2018 January 8

Abstract

We investigate the atmospheric dynamics of terrestrial planets in synchronous rotation within the habitable zone of low-mass stars using the Community Atmosphere Model. The surface temperature contrast between the day and night hemispheres decreases with an increase in incident stellar flux, which is opposite the trend seen in gas giants. We define three dynamical regimes in terms of the equatorial Rossby deformation radius and the Rhines length. The slow rotation regime has a mean zonal circulation that spans from the day to the night sides, which occurs for planets around stars with effective temperatures of 3300–4500 K (rotation period >20 days), with both the Rossby deformation radius and the Rhines length exceeding the planetary radius. Rapid rotators have a mean zonal circulation that partially spans a hemisphere and with banded cloud formation beneath the substellar point, which occurs for planets orbiting stars with effective temperatures of less than 3000 K (rotation period <5 days), with the Rossby deformation radius less than the planetary radius. In between is the Rhines rotation regime, which retains a thermally direct circulation from the day side to the night side but also features midlatitude turbulence-driven zonal jets. Rhines rotators occur for planets around stars in the range of 3000–3300 K (rotation period ∼5–20 days), where the Rhines length is greater than the planetary radius but the Rossby deformation radius is less than the planetary radius. The dynamical state can be observationally inferred from a comparison of the morphologies of the thermal emission phase curves of synchronously rotating planets.

Key words: astrobiology – planets and satellites: atmospheres – planets and satellites: terrestrial planets – stars: low-mass

1. Introduction

M-dwarf stars provide an abundance of environments for potentially hosting habitable planets. The discoveries of Proxima Centauri b around our closest stellar neighbor (Anglada-Escudé et al. 2017) and of the seven planets of the TRAPPIST-1 system (Gillon et al. 2017) indicate that M dwarfs can harbor terrestrial plants within their liquid water habitable zones (Kasting et al. 1993; Selsis et al. 2007; Kopparapu et al. 2013, 2014; Yang et al. 2013, 2014), which makes them likely candidates for upcoming surveys with *JWST* and *TESS*. Due to the small size of their host stars and their short-period orbits, habitable planets around M-dwarf stars are optimal targets for the detection and characterization of their atmospheres.

Speculation that planets in orbit around low-mass stars would be prone to synchronous rotation—so that one side experiences permanent day, while the other experiences permanent night—initially raised concern that such planets would be prone to freeze out their atmospheres and thus might not be habitable at all (Dole 1964). But subsequent investigations with simplified climate models (Haberle et al. 1996) and general circulation models (GCMs; Joshi et al. 1997; Joshi 2003; Merlis & Schneider 2010; Showman et al. 2010, 2013; Edson et al. 2011; Leconte et al. 2013; Yang et al. 2013, 2014; Carone et al. 2014, 2015, 2016; Cullum et al. 2014; Hu & Yang 2014; Way et al. 2015; Wordsworth 2015; Kopparapu et al. 2016, 2017; Fujii et al. 2017; Noda et al. 2017) have demonstrated that energy transport from the day to night hemispheres is generally sufficient to avoid atmospheric collapse across a wide range of atmospheric compositions and rotation periods.

Further analysis has revealed common patterns in the large-scale dynamics of synchronously rotating terrestrial planets, most notably a transition between circulation regimes as a planet's rotation period decreases and the Rossby deformation radius approaches the planetary radius (Merlis & Schneider 2010; Showman et al. 2010, 2013; Edson et al. 2011; Leconte et al. 2013; Yang et al. 2013, 2014; Carone et al. 2014, 2015, 2016; Haqq-Misra & Kopparapu 2015; Noda et al. 2017). For an Earth-size synchronously rotating planet, this transition occurs at a rotation period of ∼5 days (Edson et al. 2011; Carone et al. 2015). Recently, Noda et al. (2017) explored the dependence of large-scale dynamics on a wide range of rotation periods and identified four distinct dynamical regimes for synchronously rotating terrestrial planets, some of which are not explained by changes in the Rossby deformation radius alone.

In this paper, we discuss the dynamical regimes that characterize the atmospheres of habitable moist terrestrial planets in synchronous rotation around M-dwarf stars. Using the simulations conducted by Kopparapu et al. (2017), we examine the temperature contrast between the day and night sides as these planets move toward the inner edge of the

habitable zone. We then define three distinct dynamical regimes based upon the equatorial Rossby deformation radius and the Rhines length, which describe the most salient features of a planet's large-scale atmospheric dynamics. Such dynamical states could potentially be distinguished in future missions through observations of thermal emission phase curves.

2. Model Description

The set of GCM simulations by Kopparapu et al. (2017) represent Earth-sized terrestrial planets with 1 bar N_2 atmospheres, where water vapor is the only greenhouse gas. The planets are assumed to be aquaplanets covered in a swamp ocean; thus, water is abundant in the system, limited only by the Clausius–Clapeyron relation. Calculations are performed at increasing stellar flux up to the inner edge of the habitable zone, where the model atmosphere becomes unstable with the initiation of a runaway greenhouse effect. Simulated planets have global mean surface temperatures ranging between ~250–310 K. This set of calculations is conducted with six different spectral energy distributions representing a range of M-dwarf host stars, with effective temperatures of 4500, 4000, 3700, 3300, 3000, and 2600 K using the BT-SETTL grid of models (Allard et al. 2007).

We assume all planets are in synchronous rotation with their host stars. This implies that the rotation period and orbital period must be equal, which we calculate self-consistently for each case using Kepler's third law (Wordsworth 2015; Kopparapu et al. 2016, 2017) as

$$P = \left[\left(\frac{L_\star}{L_\odot}\right)\left(\frac{F_\oplus}{F_\star}\right)\right]^{\frac{3}{4}}\left[\frac{M_\odot}{M_\star}\right]^{\frac{1}{2}}. \quad (1)$$

Here, P is the orbital (and rotational) period of the planet in years, $L_\star/L_\odot$ is the luminosity of the host star scaled by the luminosity of the Sun, $F_\star/F_\oplus$ is the incident stellar flux on the planet scaled by the incident solar flux on Earth, and $M_\star/M_\odot$ is the mass of the host star in solar mass units.

These simulations were all conducted with a modified version of the Community Atmosphere Model (CAM) from the National Center for Atmospheric Research in Boulder, Colorado. This version of CAM includes updates to the native radiative transfer by implementing a new correlated-k method based on the HITRAN 2012 database as well as increases to the infrared spectral resolution. The radiative transfer in this version of CAM is valid for N_2–H_2O atmospheres with surface pressures up to 10 bar, and the GCM dynamical core includes the contribution of condensing water vapor to the surface pressure tendency. For a detailed discussion of this implementation of CAM, see Kopparapu et al. (2017).

3. Day–Night Surface Temperature Contrast

In order to detail the effectiveness of the day–night energy transport across our simulation set, we examine the surface temperature difference between the day-side and night-side hemispheres. Let $T_{\rm day}$ be the area-weighted surface temperature over the day-side (substellar) hemisphere and $T_{\rm night}$ be the area-weighted surface temperature over the night-side (antistellar) hemisphere. We plot the day–night temperature difference versus the relative stellar flux in the left panel of Figure 1, which shows that the day–night temperature difference decreases as a planet warms. Figure 1 includes markers at each of the GCM simulations conducted, labels for each stellar spectral type (left panel), labels for the rotation period (right panel), and the stellar flux scaled relative to the present-day solar flux, S_0. These simulations represent climate states ranging from the middle to the inner edge of the habitable zone for 1 bar N_2–H_2O atmospheres in synchronous rotation.

Previous studies using gray (i.e., non-wavelength-dependent) radiative transfer have suggested that the day–night temperature difference shows no dependence on the rotation period for cloud-free atmospheres (Merlis & Schneider 2010; Noda et al. 2017). Other studies have demonstrated that the presence and pattern of clouds depend on rotation period, which alters the pattern of incident stellar radiation absorbed at the surface (Yang et al. 2014; Kopparapu et al. 2016, 2017). Such experiments that separate the effects of incident stellar flux, stellar spectrum, and rotation period are instructive for improving the theoretical understanding of planetary atmospheres; however, Equation (1) states that the stellar flux and rotation period are inseparably linked for any synchronously rotating planets that are observed. Our goal with this paper is to attempt to apply the knowledge gained from these previous theoretical investigations toward the astronomically self-consistent set of GCM simulations by Kopparapu et al. (2017).

The left panel of Figure 1 shows that at a fixed value of relative stellar flux, planets around hotter stars have a larger value of day–night temperature difference. This increased day–night temperature difference occurs due to changes in both the rotation period and spectral energy distribution. These two effects are difficult to separate and can only be accounted for in a GCM with non-gray (i.e., wavelength-dependent) radiative transfer. Although rotation period by itself is insufficient to explain the changes in the day–night temperature difference, it remains a contributing factor when comparing synchronously rotating terrestrial planets around stars with different effective temperatures.

The right panel of Figure 1 shows that the equilibrium temperature, $T_{\rm eq}$, increases as the relative stellar flux increases, where $T_{\rm eq}^4 = S(1-\alpha)/4\sigma$ (where S is the stellar flux, α is the top-of-atmosphere albedo, and σ is the Stefan–Boltzman constant). Equilibrium temperature is a measure of the energy balance of the planet, with the contributions of dynamical and physical processes to radiation balance (such as clouds and surface albedo) encapsulated in the planetary albedo parameter, α. We note that hotter stars have a lower equilibrium temperature than cooler stars (when S/S_0 is constant), which occurs because cooler stars emit a lower percentage of visible radiation that can be absorbed at the planet's surface. In our discussion that follows, we scale our temperature differences by $T_{\rm eq}$ in order to show the relative contribution of direct stellar warming compared to atmospheric warming.

We define the day–night temperature contrast as $(T_{\rm day}-T_{\rm night})/T_{\rm eq}$ (following the same approach in Koll & Abbot 2016), which provides a non-dimensional parameter for comparing simulations with different host stars. We plot this day–night temperature contrast in the top-left panel of Figure 2 as a function of relative stellar flux, where higher values represent greater day–night contrast. The day–night temperature contrast (top-left panel of Figure 2), which shows a similar functional morphology to the day–night temperature difference (left panel of Figure 1), decreases as the relative stellar flux increases.

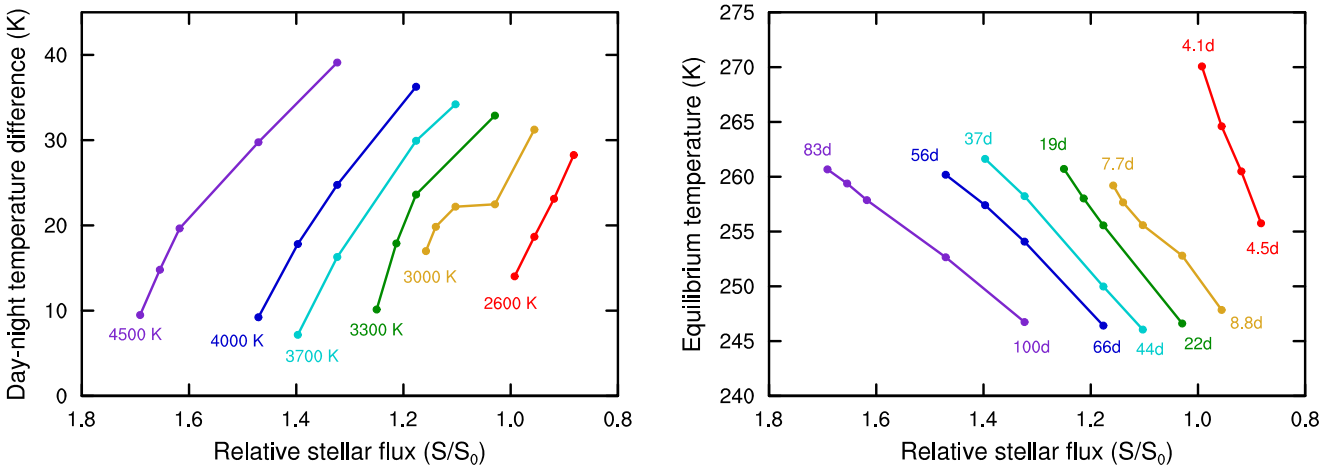

Figure 1. Full set of simulations shown as a function of relative stellar flux, S/S_0, with labels indicating the stellar effective temperature of the host star (left) and the rotation period of the planet (right), and warmer stars on the left side of the panel. As the model atmosphere warms due to an increase in S/S_0, the day–night temperature difference, $T_{\rm day}$–$T_{\rm night}$, decreases (left), while the equilibrium temperature, $T_{\rm eq}$, increases (right).

We next consider how the mean surface temperature in our simulations compares with the day–night temperature contrast. The top-right panel of Figure 2 shows that all planets in our simulation set exhibit a decrease in the day–night temperature contrast as the global mean surface temperature increases. All cases in the simulation set show a strong correlation between the day–night temperature contrast and mean surface temperature, with the warmest simulations showing the smallest day–night temperature contrast. (Here and elsewhere, we reverse the horizontal axis so that the warmest simulations are consistently on the left side of the panel.) The decrease in the day–night temperature contrast correlates with a rise in total greenhouse effect as the stellar flux increases, where the total greenhouse effect, $F_{\rm GH}$, is calculated as the difference between the surface outgoing longwave flux and top-of-atmosphere infrared flux, $F_{\rm OLR}$, so that

$$F_{\rm GH} = \sigma T_s^4 - F_{\rm OLR}. \quad (2)$$

Equation (2) suggests two possibilities causing a change in the greenhouse effect as stellar flux increases. Dry energy transport that yields a net warming provides one mechanism that can increase T_s and thus increase $F_{\rm GH}$. Moist processes provide a second mechanism, with the accumulation of water vapor (the only greenhouse gas in our simulations) causing a decrease in $F_{\rm OLR}$ that likewise increases $F_{\rm GH}$. The bottom-left panel of Figure 2 shows that the difference in greenhouse effect between the day side and the night side decreases as the planet warms. That is, as stellar flux increases for these planets, the magnitude of the greenhouse effect approaches equality between the day and night hemispheres.

The dry contribution to the decrease in the day–night temperature contrast can be explained by an increase in the static energy flux convergence on the night side. The static energy, s, is the sum of an air parcel's internal energy, c_pT (i.e., enthalpy), potential energy due to gravity, Φ, and latent energy due to moisture, L_vq. (Here, c_p is the heat capacity of air at constant pressure, Φ is the geopotential, L_v is the enthalpy of vaporization of water, and q is the specific humidity.) The static energy flux, $\boldsymbol{v}s$, represents the change in static energy due to wind (where $\boldsymbol{v}$ is the horizontal wind vector), while the static energy flux convergence, $-\nabla\cdot(\boldsymbol{v}s)$, describes the inward flow of static energy. An increase in static energy flux convergence on the night side will lead to an increase in internal energy, which, by Equation (2), causes $F_{\rm GH}$ to increase. Ultimately, this increase in static energy flux convergence occurs as a response to the deepening pressure contrast between the day and night hemispheres as a synchronously rotating planet warms, which increases divergence on the day side and convergence on the night side of the component of wind known as the isallobaric wind (see the Appendix for additional discussion). As these planets warm due to an increase in stellar flux, this increase in static energy flux divergence on the day side and convergence on the night side causes the temperature difference between the two hemispheres to decrease.

The bottom-right panel of Figure 2 shows the vertically integrated static energy flux convergence per unit mass on the night hemisphere. This quantity increases as the day–night temperature contrast decreases, which corresponds to a similar increase in the vertically integrated static energy flux divergence on the day hemisphere (not shown). The solid lines in this figure show the flux convergence with only the dry components of static energy ($c_pT+\Phi$), while the dashed lines indicate the static energy flux convergence with moisture included ($c_pT+\Phi+L_vq$). The dry static energy dominates the flux convergence, with minimal effects of latent heating evident only in the warmest simulations. For most simulations, the moist (dashed) static energy flux convergence cannot be distinguished from the dry (solid) static energy flux convergence, which reveals that the contribution of the static energy flux convergence to the day–night temperature contrast is an inherently dry phenomenon that does not necessarily depend upon latent heating from the moisture.

Many of our simulations also feature a night-side temperature inversion above the surface (up to about 800 hPa). Such inversion layers also appear in other GCM simulations of synchronously rotating atmospheres (Joshi et al. 1997; Merlis & Schneider 2010; Leconte et al. 2013) and can be replicated in simpler radiative–convective subsiding models (Koll & Abbot 2016). Note that similar temperature inversions are observed in the cold, dry, and dark polar winters on Earth (Curry et al. 1996; Liu et al. 2006), which provide an analogue to the dark antistellar hemispheres of synchronously rotating worlds. In such cases, the atmosphere radiates from the layer

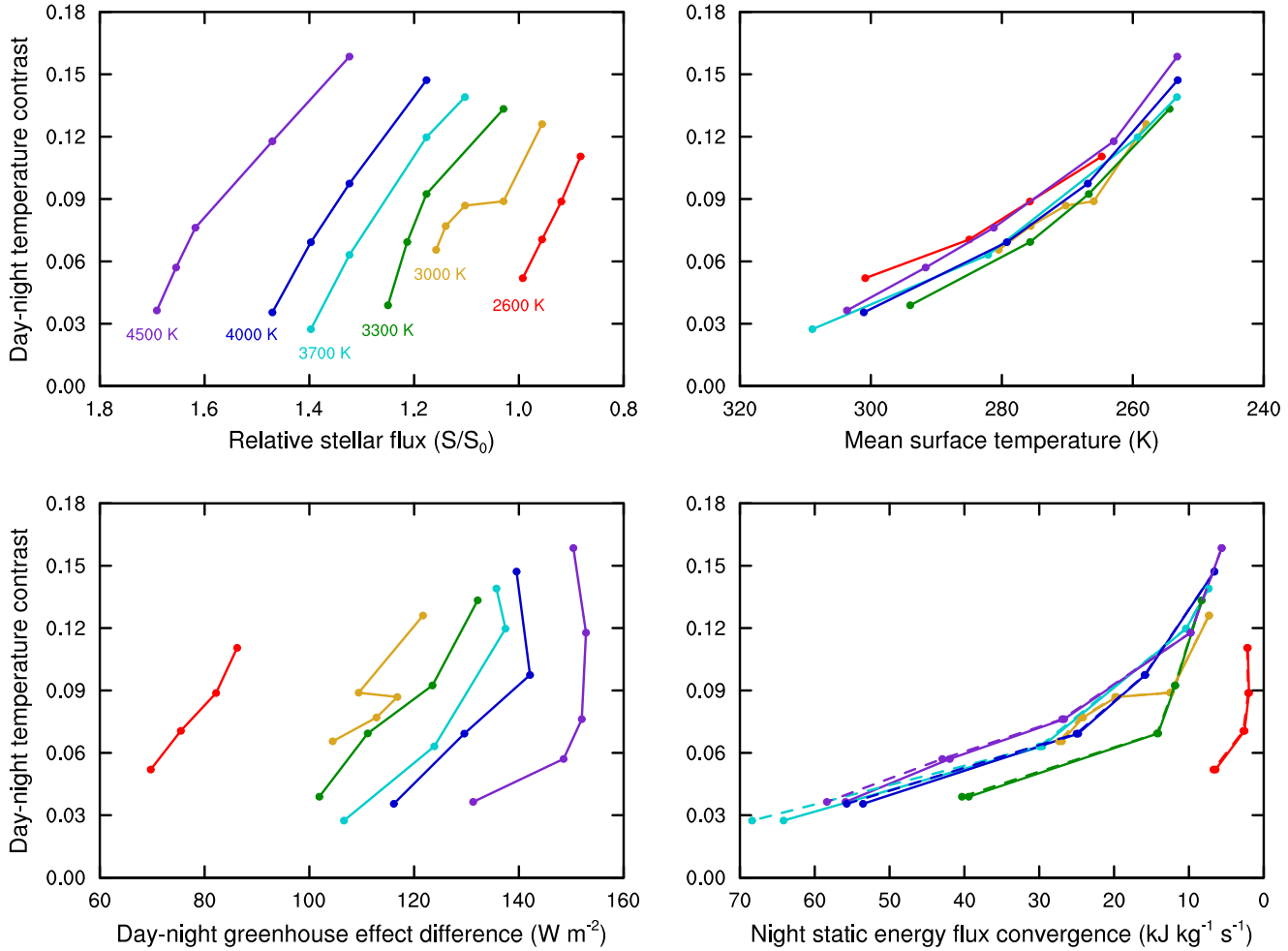

Figure 2. Full set of simulations shown as the scaled day–night temperature contrast, $(T_{day}-T_{night})/T_{eq}$, vs. relative stellar flux, S/S_0, with warmer stars on the left side of the panel (top left). These simulations all show a correlation between the scaled day–night temperature contrast and mean surface temperature (top right). This decrease in day–night temperature contrast as the planet warms corresponds to a decrease in the day–night greenhouse effect difference (bottom left), which occurs as a result of an increase in the the dry static energy flux convergence on the night side (bottom right, solid lines). The total static energy, with the moist latent energy component included, is also shown (bottom right, dashed lines), but the contribution of this latent energy is very small.

above this inversion, which provides additional infrared flux into the surface and can even contribute to a negative net greenhouse effect, $F_{GH} < 0$, for some of the coldest simulations. The inversions, both for antistellar hemispheres and for polar winters on Earth, are maintained by vigorous radiative cooling of land and ice surfaces along with the transport of overlying warmer air masses in the free atmosphere (Bintanja et al. 2011).

Unlike Earth's poles, the antistellar hemispheres of synchronously rotating planets always remain dark, and thus the inversion can be a permanent feature. However, the night-side inversion decreases in strength as the planet warms, with the destruction of the inversion triggered by the increase in dry static energy flux convergence on the night side near the surface (Figure 2). Warming of the night-side surface layers from dry static energy convergence then increases the water vapor abundance, which increases the night-side water vapor greenhouse effect and causes further warming. Here, we find that the night-side inversions vanish for planets with mean surface temperatures of $\geqslant$300 K. Water vapor increases in both hemispheres as stellar flux increases and the surface warms. While the absolute magnitude of greenhouse effect increases all across the planet as the atmosphere warms, the difference in the greenhouse effect between day and night side lessens, which contributes to the reduction of the day–night temperature contrast.

3.1. Comparison with Gray Analytic Theory

The contributions from water vapor accumulation and dry energy transport to the total greenhouse warming in Equation (2) can be represented as an equivalent optical gray depth, which summarizes this combined warming in a parameter that can be compared with the gray analytic theory. Koll & Abbot (2016), following a similar approach to Wordsworth (2015), analyze the atmospheres of dry synchronously rotating planets by drawing upon Carnot's theorem to describe the scaling of surface winds as a heat engine. Using a gray analytic two-column model, Koll & Abbot (2016) develop expressions for T_{day} and T_{night},

$$T_{day} \approx 2^{1/4} T_{eq} \left[1 - \frac{3\tau_{LW}}{4\left(1 + 4\frac{R}{c_p}\right)} \right] \quad (3)$$

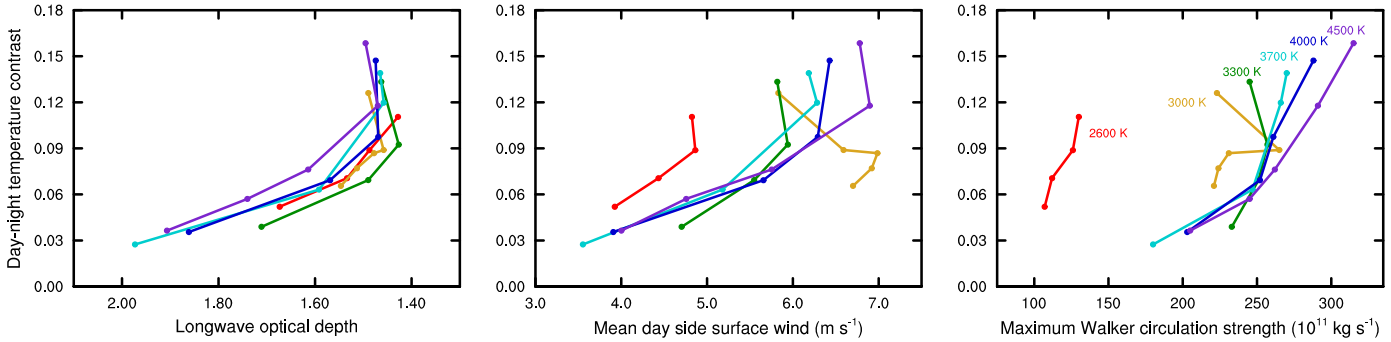

Figure 3. Longwave equivalent gray optical depth calculated from Equations (3) and (4) showing these model atmospheres become increasingly optically thick as the planet warms and the day–night temperature contrast shrinks (left). The mean day-side surface wind (middle) and maximum strength of the Walker circulation (right) both tend to decrease as the planet warms. Note that the 2600 and 3000 K cases show significant differences from the other simulations.

and

$$T_{\rm night} \approx 2^{1/4} T_{\rm eq} \frac{\tau_{\rm LW}^{1/4}}{\left(1 + 4\frac{R}{c_p}\right)^{1/4}}, \quad (4)$$

where $\tau_{\rm LW}$ is the globally averaged longwave optical depth and R is the dry gas constant. Equation (3) shows that the day-side temperature decreases with $\tau_{\rm LW}$, while Equation (4) reveals that the night-side temperature increases with $\tau_{\rm LW}$. Combining Equations (3) and (4) to obtain $(T_{\rm day}-T_{\rm night})/T_{\rm eq}$ shows that the day–night temperature contrast decreases as $\tau_{\rm LW}$ increases. This remains consistent with our model results that show an increase in greenhouse effect, analogous to an increase in $\tau_{\rm LW}$, associated with the decrease in the day–night temperature contrast.

Substituting values of $(T_{\rm day}-T_{\rm night})/T_{\rm eq}$ from our results into Equations (3) and (4) allows us to calculate an equivalent gray optical depth for our set of GCM calculations, which we show in the left panel of Figure 3. In our case, the parameter $\tau_{\rm LW}$ represents any process that contributes to greenhouse warming (Equation (2)), which includes both the accumulation of water vapor and increase in static energy flux convergence as stellar flux increases, as well as cloud processes. Although the analytic model of Koll & Abbot (2016) focuses on dry atmospheres, this relationship between $\tau_{\rm LW}$ and $F_{\rm GH}$ still remains qualitatively consistent with our non-gray, moist GCM results.

The Koll & Abbot (2016) heat engine analogy is continued by predicting that the mean day-side surface wind, U_s, should scale as $U_s^3 \sim (T_{\rm day}-T_{\rm eq})(1-e^{-\tau_{\rm LW}})T_{\rm eq}^4$. This expression, and a similar one developed by Wordsworth (2015), compares favorably with the dry GCM calculations that use gray radiative transfer; however, applying this relationship to our moist GCM results by substituting from Equations (3) and (4) suggests that U_s should increase as the planet warms. However, Figure 3 (middle panel) shows the U_s calculated from our GCM simulations as the area-weighted root mean squared surface wind on the day hemisphere, which indicates that the simulations with the smallest day–night temperature contrast have the smallest value of mean day-side wind. Figure 2 (upper left) shows that these simulations with the smallest day–night temperature contrast also show the warmest mean surface temperatures. This implies that U_s in our simulations tends to decrease as a planet moves toward the inner edge of the habitable zone and the day–night temperature contrast shrinks. Likewise, the strength of the zonal overturning (i.e., Walker) circulation also tends to decrease as the planet moves toward the inner edge of the habitable zone (Figure 3, right panel). These results from our moist GCM simulations are somewhat inconsistent with dry analytic theory, showing a decrease in wind speed and zonal circulation strength, due to changes in both stellar insolation and planetary rotation period.

The theoretical expression of Koll & Abbot (2016) remains valid when we examine our results at a fixed value of day–night temperature contrast. Figure 3 shows that at a fixed value of day–night temperature contrast (e.g., $(T_{\rm day}-T_{\rm night})/T_{\rm eq} = 0.12$), the mean day-side surface wind increases with stellar effective temperature (middle panel) as does the maximum Walker circulation strength (right panel). Stars with a higher stellar effective temperature emit a higher proportion of energy at shorter wavelengths, which corresponds to additional surface heating on planets orbiting such stars.

Water vapor absorption is one key feature present in our GCM that is absent in the gray analytic model of Koll & Abbot (2016). Stars with a lower stellar effective temperature have stronger emission at infrared wavelengths, which allows for greater absorption of this incoming radiation by water vapor in the atmosphere. This effect is evident in Figure 3: planets orbiting the hottest stars are largely transparent to incoming stellar radiation, which causes greater surface warming and leads to the strongest circulation and surface winds. Likewise, planets orbiting cooler stars absorb a larger fraction of incoming radiation, which causes less direct surface warming and leads to a reduction in the maximum Walker circulation strength.

In general, the analytic expressions by Koll & Abbot (2016) can adequately describe variations in U_s for large changes in $\tau_{\rm LW}$ (such as comparing planets with fixed day–night temperature contrast around stars of different spectral types), but this relationship breaks down when considering the smaller changes in surface pressure and wind that occurs as a terrestrial planet moves closer toward the inner edge of the habitable zone.

3.2. Comparison with Gas Giants

The day–night temperature contrast is one of the primary observable features of exoplanet atmospheres. The decreasing trend of the day–night surface temperature contrast with increasing equilibrium temperature from our terrestrial simulations is opposite for synchronously rotating gas giant planets, where observations show that an increase in heating leads to an increase in the day–night temperature contrast (Perez-Becker &

Showman 2013; Komacek & Showman 2016; Komacek et al. 2017). The day–night temperature contrast observed in an optically thick gas giant atmosphere occurs at the emission level in the free atmosphere, whereas the flux emitted by an optically thin terrestrial atmosphere primarily emerges from the surface. These opposite trends imply that the two types of atmospheres are located in two fundamentally different regimes: a hot, dry, top-heated gas giant regime versus a cold, moist, bottom-heated terrestrial regime.

For both of these regimes, the day–night heat transport in the free atmosphere of synchronously rotating planets is strongly influenced by radiation and zonally propagating waves (Perez-Becker & Showman 2013; Showman et al. 2013; Koll & Abbot 2015, 2016; Wordsworth 2015; Komacek & Showman 2016; Komacek et al. 2017; Zhang & Showman 2017). The free-atmosphere day–night temperature contrast can be predicted based on a scaling theory developed by Komacek & Showman (2016), Komacek et al. (2017), and Zhang & Showman (2017),

$$\left.\frac{T_{\rm day}-T_{\rm night}}{T_{\rm eq}}\right|_{\rm free} \sim 1-\frac{2}{\alpha+\sqrt{\alpha^2+4\gamma^2}}, \quad (5)$$

where the non-dimensional parameters α and γ are defined as

$$\alpha = 1+\frac{\left(\Omega+\frac{1}{\tau_{\rm drag}}\right)\tau_{\rm wave}^2}{\tau_{\rm rad}\Delta\ln p}, \quad (6)$$

$$\gamma = \frac{\tau_{\rm wave}^2}{\tau_{\rm rad}\tau_{\rm adv,eq}\Delta\ln p}. \quad (7)$$

Here, Ω is the rotation rate, $\tau_{\rm rad}$ is the radiative timescale, $\tau_{\rm wave}$ is the timescale for wave propagation, $\tau_{\rm drag}$ is the frictional drag timescale, $\Delta\ln p$ is the thickness of the photosphere in terms of log pressure, and $\tau_{\rm adv,eq}$ is the advective timescale due to the "equilibrium cyclostrophic wind." (See Appendix A from Zhang & Showman 2017 for more information.)

The key parameters here are the radiative timescale, $\tau_{\rm rad}$, and wave propagation timescale, $\tau_{\rm wave}$. The typical radiative timescale on a canonical hot Jupiter is about 10^4–10^6 s in the photosphere (Showman & Guillot 2002). The gravity wave speed, $(gH)^{1/2}$, where g is gravitational acceleration and H is scale height, is on the order of 1 km s^{-1}, resulting in a wave propagation timescale of 10^4–10^5 s, which is comparable to the radiative timescale. However, the temperature dependence of the two timescales is different. In the dry atmosphere of a gas giant, $\tau_{\rm rad}\propto T_{\rm eq}^{-3}$ (Showman & Guillot 2002) if opacity does not significantly change with temperature. On the other hand, in an isotherm limit, $\tau_{\rm wave}\propto T_{\rm eq}^{-1}$. As equilibrium temperature increases, the radiative timescale decreases more rapidly than the wave propagation timescale. Equation (5) predicts that the day–night temperature contrast will increase. Physically, the atmosphere of a gas giant will become more radiation controlled and the day–night heat transport will be less efficient because of waves, which results in a larger day–night temperature contrast. Simulations by Komacek & Showman (2016) and Komacek et al. (2017) have confirmed this trend in the hot atmosphere regime for giant planets.

By contrast, due to their colder temperature and smaller planetary radius, terrestrial atmospheres in the habitable zone generally show a much shorter wave propagation timescale compared to the radiative timescale (Selsis et al. 2011; Koll & Abbot 2015). For example, a typical radiative timescale on an Earth-like planet is a few days, but the gravity wave propagation timescale is about an hour due to its smaller planetary radius. Thus, the ratio $\tau_{\rm wave}/\tau_{\rm rad}$ is on the order of 0.01 or less (Koll & Abbot 2015). This implies that the temperature of the day side and night side are homogenized in the free atmosphere, which leads to the "weak temperature gradient" regime for terrestrial atmospheres (Koll & Abbot 2015, 2016; Wordsworth 2015). Unlike the gas giant regime, which are primarily heated from the top, the atmospheres of optically thin terrestrial planets are primarily heated from the bottom. Surface temperatures, both on the day and night sides, are approximately in radiative–convective equilibrium with the overlying atmospheres (Koll & Abbot 2016). As a result, the day–night surface temperature contrast in the terrestrial regime is primarily governed by the opacity that controls the surface-atmosphere radiative flux exchange, as shown by Equations (3) and (4). Given a particular stellar flux, increasing the opacity will tend to decrease the day-side surface temperature but increase the night-side surface temperature (Koll & Abbot 2016), which therefore decreases the day–night temperature contrast at surface. If opacity does not change significantly with equilibrium temperature in the dry atmosphere, the day–night temperature contrast will be approximately constant for all planets. In thin moist atmospheres, the presence of water vapor, and its associated increase in longwave opacity with equilibrium temperature, leads to a decreasing trend of the day–night surface temperature contrast.

4. Dynamical Regimes

We analyze three regimes for large-scale atmospheric dynamics on synchronously rotating planets—slow rotators, rapid rotators, and Rhines rotators—and their dependence on the Rossby deformation radius and the Rhines length. We define and discuss the relevant dynamical parameters for each of these cases below, which we compare with previous GCM studies that have examined the dynamical regimes of synchronously rotating planets. We show that terrestrial planets in the habitable zone of stars with an effective stellar temperature of 3700–4500 K are in the slow rotation regime, while those around 2600 K stars are in the rapid rotation regime. Intermediate stellar cases in the range of 3000–3300 K show a unique transitional dynamical state that we describe as the Rhines rotation regime.

These three dynamical regimes are defined using two parameters: the Rossby deformation radius, which constrains the maximum extent of the zonal overturning circulation, and the Rhines length, which determines the maximum extent of zonally elongated turbulent structures. We summarize this approach for characterizing the atmospheric dynamics of a synchronously rotating planet in Figure 4. Slow rotators are found in the upper-right quadrant of Figure 4, where the non-dimensional Rossby deformation radius and the non-dimensional Rhines length are both greater than one. Rapid rotators occur in the lower-left quadrant of Figure 4, where both the non-dimensional Rossby deformation radius and non-dimensional Rhines length are less than one. Rhines rotators describe a transitional dynamical state, which occurs in the lower-right quadrant of Figure 4 with a non-dimensional Rossby deformation radius greater than one but a non-dimensional Rhines length less than one. We apply these regimes below in our discussion of terrestrial planets near the

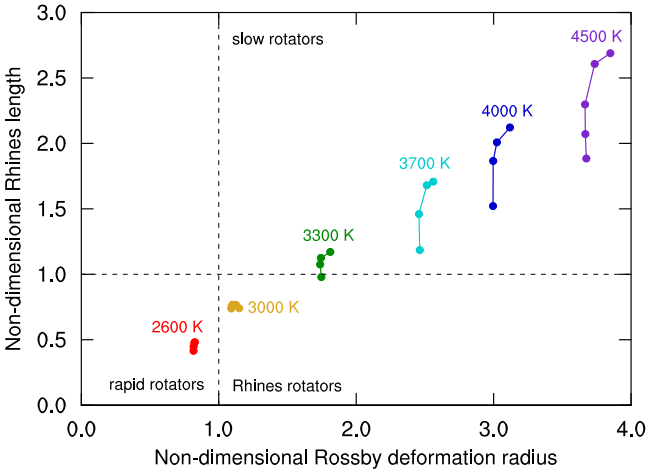

Figure 4. Synchronously rotating planets are in the rapid rotation regime when the non-dimensional Rossby deformation radius is less than one, $\lambda_R/a < 1$, which includes all 2600 K simulations. The Rhines rotation regime occurs when the non-dimensional Rhines length is less than one but the non-dimensional Rossby deformation radius is greater than one, $L_R/a < 1$ and $\lambda_R/a > 1$, which includes all 3000 K simulations and one 3300 K case. Planets in the slow rotation regime have both $\lambda_R/a > 1$ and $L_R/a > 1$, which describe the remaining simulations for stars 3300–4500 K.

inner edge of the habitable zone, but this classification scheme can be generalized to planets with less Earth-like atmospheres, including synchronously rotating giant planets.

4.1. Slow Rotators

Slow rotators are characterized by strong convective motion beneath the substellar point, with energy transport by Rossby and Kelvin waves from the day to the night side of the planet. Atmospheric dynamics on a slow rotator are broadly characterized by a thermally direct circulation with heating and rising air on the day side, cooling and descending air on the night side, and the strength of the circulation limited by frictional dissipation in the boundary layer (Koll & Abbot 2016). Slow rotators are equivalent to the "Type-I" circulation regime described by Noda et al. (2017), where the thermally direct day–night circulation is the primary characteristic of the planet's large-scale dynamics.

Previous studies have demonstrated that maintaining this hemispheric large-scale circulation requires the Rossby deformation radius be greater than the planetary radius (Merlis & Schneider 2010; Showman et al. 2010, 2013; Edson et al. 2011; Leconte et al. 2013; Carone et al. 2014, 2015, 2016; Yang et al. 2014; Haqq-Misra & Kopparapu 2015; Noda et al. 2017). The Rossby deformation radius represents the ratio of buoyancy to rotational forces. For synchronously rotating planets, the Rossby deformation radius is proportional to the maximum extent of the mean zonal circulation from the day to the night side. Because we are primarily concerned with the equatorial propagation of Rossby, Kelvin, and other waves, we focus on the equatorial Rossby radius of deformation, λ_R, which we express, following Gill (1982), as

$$\lambda_R = \sqrt{\frac{gH}{2\beta}}, \tag{8}$$

where H is the atmospheric scale height, $\beta = 2\Omega$ represents the Coriolis parameter at the equator, and $g = 9.81\ \mathrm{m\ s^{-2}}$. We express the scale height as $H = \bar{T}_s R/m_{\mathrm{air}} g$, where $\bar{T}_s$ is the global mean surface temperature and $m_{\mathrm{air}} = 0.028\ \mathrm{kg\ mol^{-1}}$ is the molar mass of air (Edson et al. 2011). Letting a be the planetary radius, we define slow rotators as planets where $\lambda_R/a > 1$. Using a present-day Earth GCM, Edson et al. (2011) noted that this definition requires that slow rotators must have a rotational period of ~5 days or greater, for an Earth-size planet in synchronous orbit around a G-dwarf star. Other studies using more idealized GCMs (Carone et al. 2014, 2015, 2016; Noda et al. 2017) have found comparable values for this limit on slow rotators. All planets in our set of simulations have a rotation period greater than 5 days, except for planets orbiting a 2600 K host star. This means that, aside from the coolest host star, all of these cases should expect to show $\lambda_R/a > 1$.

The Walker circulation for the set of simulations is shown in Figure 5, where the contours show the strength of the mean zonal circulation, and the shading shows rising motion. This particular set of simulations was chosen because they all have an approximately constant value of day–night contrast, where $(T_{\mathrm{day}} - T_{\mathrm{night}})/T_{\mathrm{eq}} \approx 0.7$. Figure 5 confirms that $\lambda_R/a > 1$ for all cases from 4500 to 3000 K, where the planet's large-scale dynamics are characterized by a thermally direct zonal circulation that spans the day–night hemisphere. All simulations with $\lambda_R/a > 1$ show the presence of this hemispheric zonal circulation, although only those cases that also show a non-dimensional Rhines number (defined in Section 4.3) greater than one are classified as slow rotators.

4.2. Rapid Rotators

Rapid rotators are characterized by weak convective motion beneath the substellar point, with a Rossby deformation radius less than the planetary radius ($\lambda_R/a < 1$; Figure 4). Rapid rotators tend to show banded cloud formation beneath the substellar point (Yang et al. 2014; Kopparapu et al. 2016) and a mean zonal circulation that only partially reaches from the day to the night side (Haqq-Misra & Kopparapu 2015; Kopparapu et al. 2017) Rapid rotators are comparable to the "Type-IV" circulation regime described by Noda et al. (2017), with some dynamical features that resemble present-day Earth.

The 2600 K case appears as an outlier in the bottom-right panel of Figure 2, which can be understood as these planets being in a rapidly rotating regime with a zonal flow that does not span the day–night hemisphere. This is shown in Figure 5, where the 2600 K case exhibits its rapid rotation through a less organized zonal circulation with a larger number of cells that do not span the day–night hemisphere. The 2600 K case also shows less direct rising motion beneath the substellar point, which leads to a reduction in the amount of convectively transported water vapor to the upper troposphere.

The set of GCM simulations is plotted in terms of rotation period versus λ_R/a in Figure 6 (left panel), which shows that only the 2600 K case falls within the rapid rotation regime. The rest of the simulations show a thermally direct circulation that spans the day to the night hemisphere. Although the 3000 K case is close to the dashed line in the left panel of Figure 6, where $\lambda_R/a = 1$, we can confidently exclude the 3000 K case from being a rapid rotator, because its Walker circulation spans from the day to the night side (Figure 5). Only when the rotation period is less than ~5 days (for Earth-mass planets) does the Walker circulation show evidence of the rapid rotation dynamical regime.

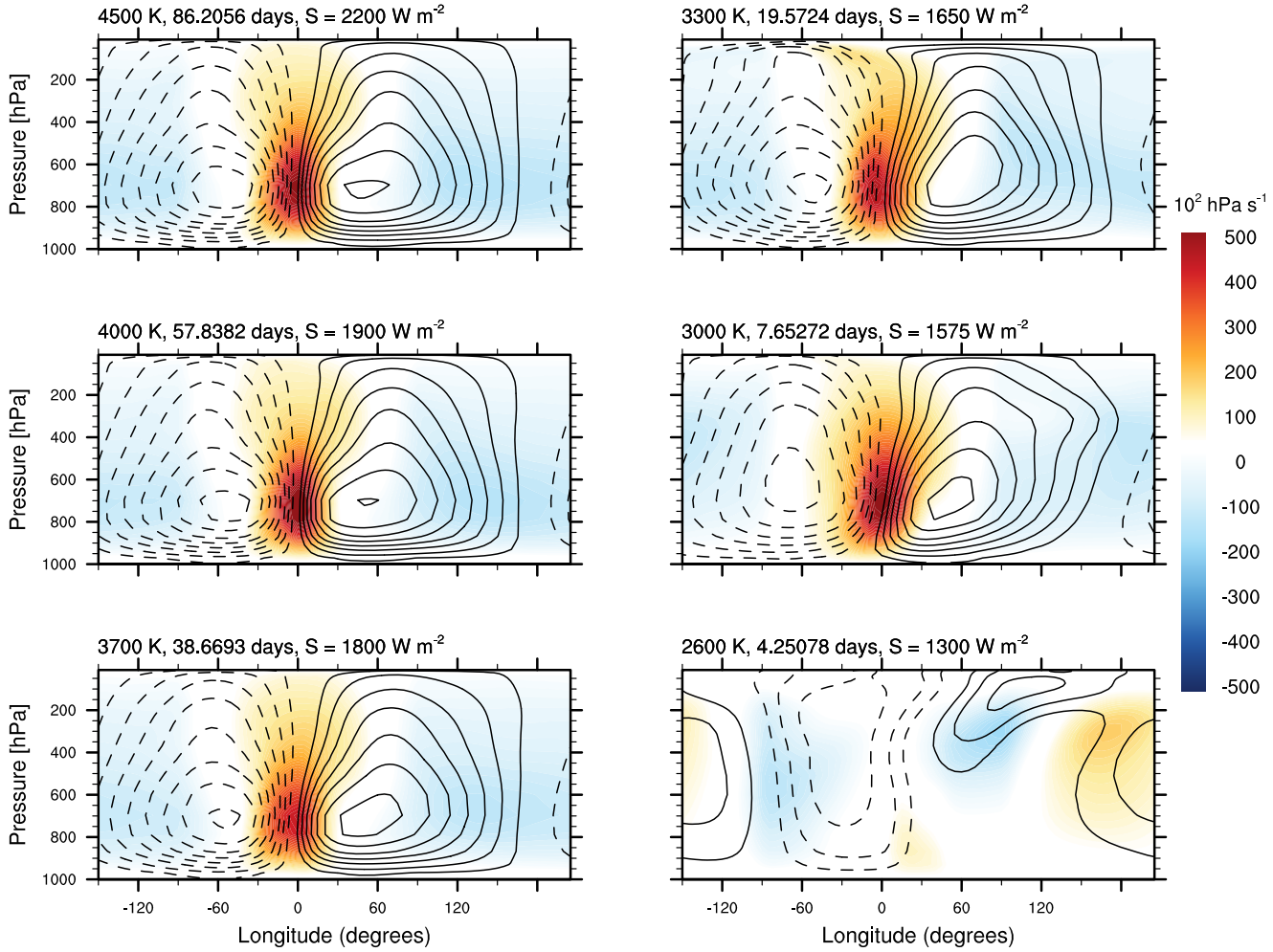

Figure 5. The Walker circulation and meridionally averaged vertical wind for synchronously rotating planets around 4500, 4000, 3700, 3300, and 3000 K stars all show a thermally direct zonal circulation that spans the day to the night side. The 2600 K case shows rapid rotation with a Walker circulation that spans less than a full hemisphere. The contour interval for the Walker circulation is 30×10^{11} kg s^{-1}, with the solid contours indicating clockwise circulation and the dashed contours indicating counterclockwise circulation. The shading indicates pressure tendency, which corresponds to rising (warm colors) or sinking (cool colors) motion.

Some studies have extended their GCM simulations to planets with a smaller rotation period of 1 day (Merlis & Schneider 2010; Carone et al. 2014, 2015, 2016; Haqq-Misra & Kopparapu 2015; Noda et al. 2017). Noda et al. (2017) even discuss a "Type-III" circulation regime that occurs at a rotation period of a few days, less than the rotational period of our 2600 K cases. We ignore these cases in our present study because Equation (1) requires that any planet with a rotation period of 1 day or less that also resides in the habitable zone of its host star must therefore reside around very cool brown dwarf stars. Because our set of calculations extends only to 2600 K stars, such planets with short 1 day or less orbital periods are beyond the scope of this study.

4.3. Rhines Rotators

Rhines rotators are characterized by strong upper-atmosphere superrotation as well as strong upwelling beneath the substellar point, occupying a transition region between slow and rapid rotators (Figure 4, lower-right quadrant). Rhines rotators still show a Walker circulation that spans the day to the night side (Figure 5), similar to slow rotators, but their atmospheric dynamics are also characterized by asymmetric zonal jets at midlatitudes. Rhines rotators are analogous to the "Type-II" circulation regime described by Noda et al. (2017), who show the point of maximum heating beginning to drift off-center from the substellar point. This transitional regime, which shows an increasing effect of equatorial superrotation dynamics, was also noted by Edson et al. (2011) and Carone et al. (2014).

Figure 7 shows the surface temperature and wind vectors for the same set of GCM simulations as in Figure 5. The 4500, 4000, and 3700 K cases all show the characteristic flow inward toward the substellar point, with the surface flow in one hemisphere a mirror image of the other. This mirror symmetry starts to break in the 3300 K case, with the beginnings of an eastward shift of the point of maximum heating. The 3000 and 2600 K cases both show a notably different flow pattern along the surface and toward the substellar point, with turbulent features contributing to both the midlatitude and equatorial flow. In particular, the vortex-like structures at midlatitude and polar latitudes of the 3000 K case in Figure 7 indicate the breaking of symmetry due to turbulent flow.

We further detail the energy distribution of our simulation set by examining the temperature difference between the substellar point at the equator and the pole. Let $T_{\rm equator}$ be the maximum temperature beneath the substellar region and $T_{\rm pole}$ be the minimum of the north and south pole temperatures.

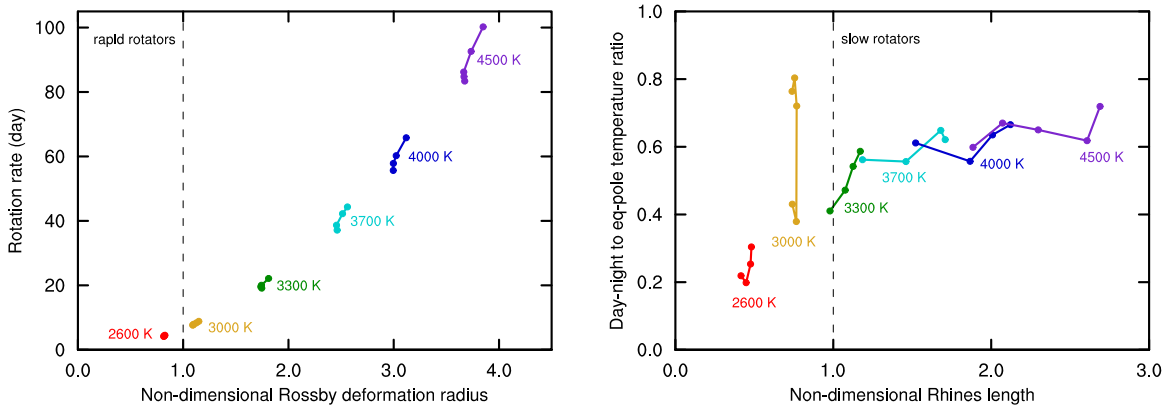

Figure 6. Synchronously rotating planets are in the rapid rotation regime when the non-dimensional Rossby deformation radius is less than one, $\lambda_R/a < 1$, which occurs at a rotation period of ∼5 days (left). The Rhines rotation regime occurs when the non-dimensional Rhines length is less than one, $L_R/a < 1$ (right). Such planets respond to an increase in stellar flux by reducing the day–night temperature to the equator-to-pole temperature ratio, $(T_{\rm day}-T_{\rm night})/(T_{\rm equator}-T_{\rm pole})$. Planets in the slow rotation regime have both $\lambda_R/a > 1$ and $L_R/a > 1$.

Figure 8 shows the equator-to-pole temperature contrast $(T_{\rm equator}-T_{\rm pole})/T_{\rm eq}$ versus relative stellar flux, mean surface temperature, the day–night greenhouse effect difference, and the vertically integrated night-side static energy flux convergence. All of the slow rotators from 4500 K through 3300 K show similar trends as Figure 2, with the magnitude of the equator-to-pole temperature contrast even greater than the magnitude of the day–night temperature contrast. By comparison, the 3000 K and 2600 K cases appear as outliers from the others in the two panels on the bottom row of Figure 8, which is due in part to their warmer poles compared to the slow rotating cases. This behavior cannot be explained by the Rossby deformation radius alone, since the 3000 K case shows $\lambda_R/a > 1$ while the 2600 K case is a rapid rotator.

Turbulent structures on Earth and other asynchronously rotating planets tend to elongate in the east–west direction compared to north–south, which Rhines (1975) realized is due to the variation in the Coriolis parameter with latitude. The latitudinal scale at which turbulent flow can organize into zonal jets is known as the Rhines length, which is defined as

$$L_R = \pi\sqrt{\frac{U}{\beta}}, \tag{9}$$

where U is a characteristic root mean squared velocity at the relevant energy-containing scale (Showman et al. 2010, 2013; Vallis 2017). In general, the Rhines scale represents the transition scale between turbulent and wave-driven motion. Turbulent structures on Earth can only grow to sizes limited by the Rhines scale, beyond which Rossby waves dynamics become the primary driver. We define a non-dimensional Rhines length, L_R/a, which indicates the zonal scale to which turbulent structures can grow. On Earth and Jupiter today, $L_R/a < 1$, thereby implying that any zonal jets that emerge from turbulent energy cannot grow to encompass the entire planetary circumference. For synchronously rotating planets, we can use this non-dimensional Rhines length to determine the conditions under which turbulence-driven zonal jets can grow to planetary scales. For $L_R/a > 1$, the length scale for the turbulent energy cascade is greater than the planetary radius, so we expect the atmospheric dynamics to be dominated by the thermally direct circulation from the day to the night side, with little contribution from turbulence-driven jets. Conversely, for $L_R/a < 1$, the length scale for the turbulent energy cascade is smaller than the planetary radius, so zonal turbulence-driven jets can form at midlatitudes and cause a departure from symmetry in the surface flow. We refer to these synchronously rotating planets, defined by $L_R/a < 1$ and $\lambda_R/a > 1$, as Rhines rotators.

Figure 6 (right panel) shows the ratio of the day–night temperature contrast to the equator-to-pole temperature contrast ratio, $(T_{\rm day}-T_{\rm night})/(T_{\rm equator}-T_{\rm pole})$, versus the non-dimensional Rhines number. Our calculation of the Rhines length assumes that U is equal to the area-weighted root mean squared surface wind on the day hemisphere, as shown in Figure 3. For all of the slow rotators from 4500 to 3700 K, we see that $L_R/a > 1$, which implies a large-scale dynamical structure characterized by a symmetric, thermally direct circulation from the day to the night side (Figure 5). By contrast, all cases for 2600 K and 3000 K stars show $L_R/a < 1$, which implies that the atmospheric dynamics of such planets include contributions at midlatitudes from turbulent-driven zonal jets that break the symmetry of surface flow when compared to slow rotators. Figure 6 also shows that the 3300 K simulation resides in a transition zone between Rhines rotation and slow rotation, where $L_R/a \approx 1$.

Figure 4 indicates the cases in our GCM simulations that fall within the Rhines rotation regime, with $L_R/a < 1$ and $\lambda_R/a > 1$. These simulations all show very little spread in the value of L_R, even though the stellar flux varies. The primary feature of planets within the Rhines rotation regime is that the atmosphere responds to an increase in stellar energy by decreasing the day–night to equator–pole temperature contrast ratio (Figure 6, right panel) by breaking zonal symmetry without changing the total kinetic energy by much. By comparison, planets in the slow rotation regime respond to an increase in stellar energy by decreasing the day–night temperature contrast as well as the root mean squared wind speed (Figure 3, right panel), which increases the total kinetic energy. Rhines rotators are able to develop zonal structures on the scale of the planetary radius, which induces the development of midlatitude and polar vortices and other transient dynamical features that break the symmetry of the thermally direct model for large-scale circulation.

We show the zonal wind and the mean meridional (i.e., Hadley) circulation (MMC) in Figure 9 for the same set of

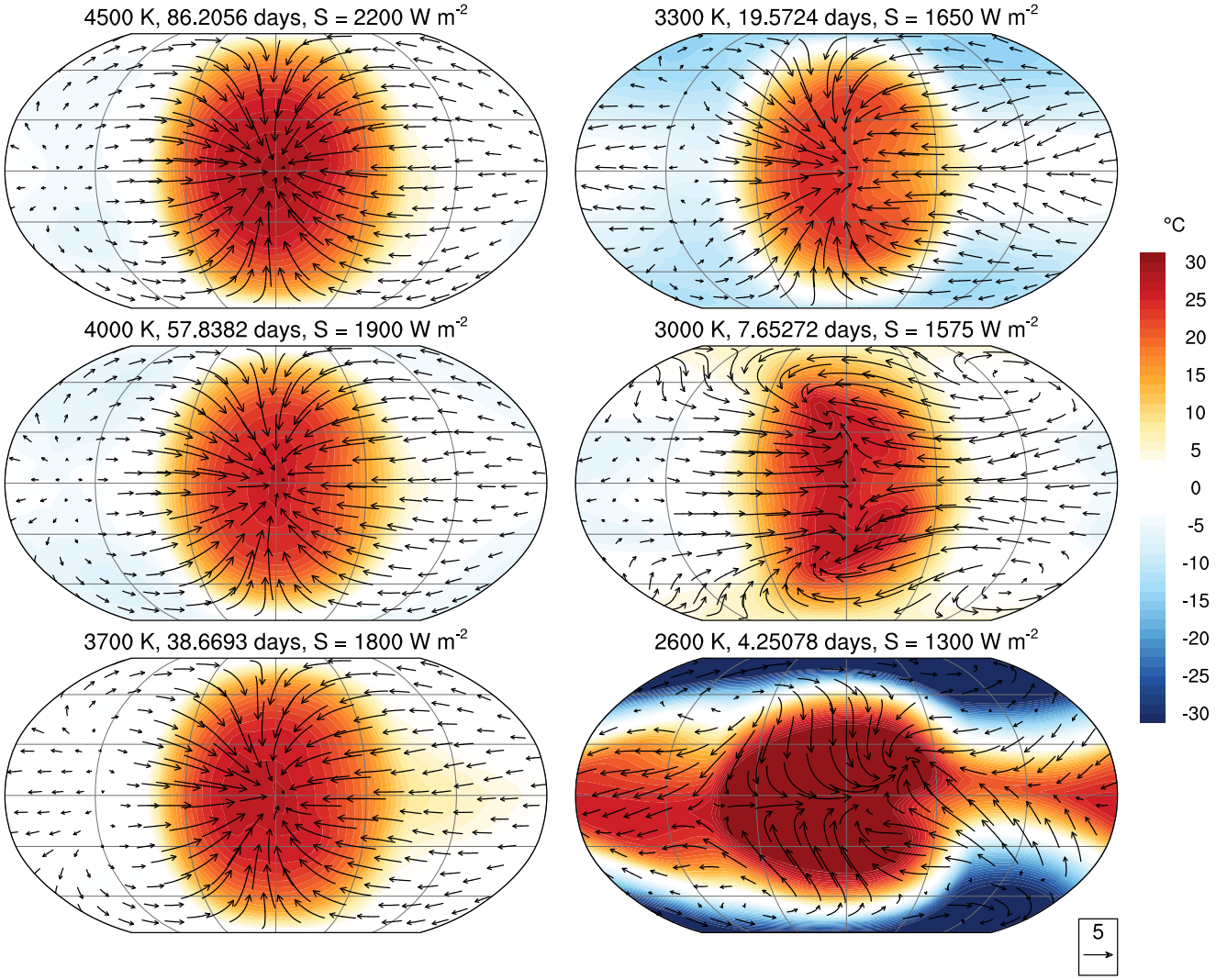

Figure 7. Surface temperature and surface wind vectors show a nearly symmetric pattern of substellar heating and flow toward the substellar point for planets in the slow rotation regime around 4500, 4000, 3700, and 3300 K stars. The 2600 K case in the rapid rotation regime shows asymmetric warming flow patterns that extend in an equatorial band from the day to the night side. In between is the Rhines regime, which shows a departure from symmetry particularly at midlatitudes for the 3000 K cases.

cases as shown in Figures 5 and 7. The left row shows the global quantities of the zonal wind and MMC, while the middle and right rows show the eastern and western hemispheres, respectively, from the substellar point. Note that the direction of the Hadley circulation changes sign when comparing the eastern and western hemispheres, as discussed by Haqq-Misra & Kopparapu (2015). This is a prediction that emerges from the simplified shallow water study of Geisler (1981), who found that the MMC changes direction on either side of a fixed heating source. This suggests that hemispheric separation of the MMC should always be examined for synchronously rotating planets, as the global mean MMC tends to cancel out branches with opposite signs of circulation on either side of the substellar point.

The 4500 K through 3700 K cases all show surface flow into the substellar point and a stronger easterly jet in the western hemisphere. By contrast, the 2600 and 3000 K cases show strong upper-atmospheric superrotation in both hemispheres. The 2600 K slow rotators show very strong superrotation at all latitudes and in both hemispheres, which is due to these planets having both $L_R/a < 1$ and $\lambda_R/a < 1$. The 3000 K case is a Rhines rotator with $L_R/a < 1$ and $\lambda_R/a > 1$, which manifests as zonal jets at the surface and middle of the atmosphere. We see the zonal propagation of Rossby waves dominating the upper atmosphere of the 3000 K cases, although an upper-level westerly jet also persists in these simulations. The 3300 K case remains at the threshold of the Rhines rotator transition, with a strong easterly jet persisting in both hemispheres and a strong westerly jet at the top of the model atmosphere.

The Rhines rotator regime represents a transitional, but distinct, dynamical state for terrestrial planets in synchronous rotation. Rhines rotators respond to an increase in stellar forcing by decreasing the equator–pole temperature contrast and are characterized by the presence of planetary-scale turbulent structures. Rhines rotators should be expected for terrestrial planets in the habitable zone of M-dwarf stars with an effective stellar temperature of 3000–3300 K.

We also note that the upper-left quadrant of Figure 4 represents a fourth regime where the Rhines length is larger than the Rossby deformation radius, although this situation did not arise in our simulations. This regime could exist in principle, but most cold atmospheres show a root mean squared

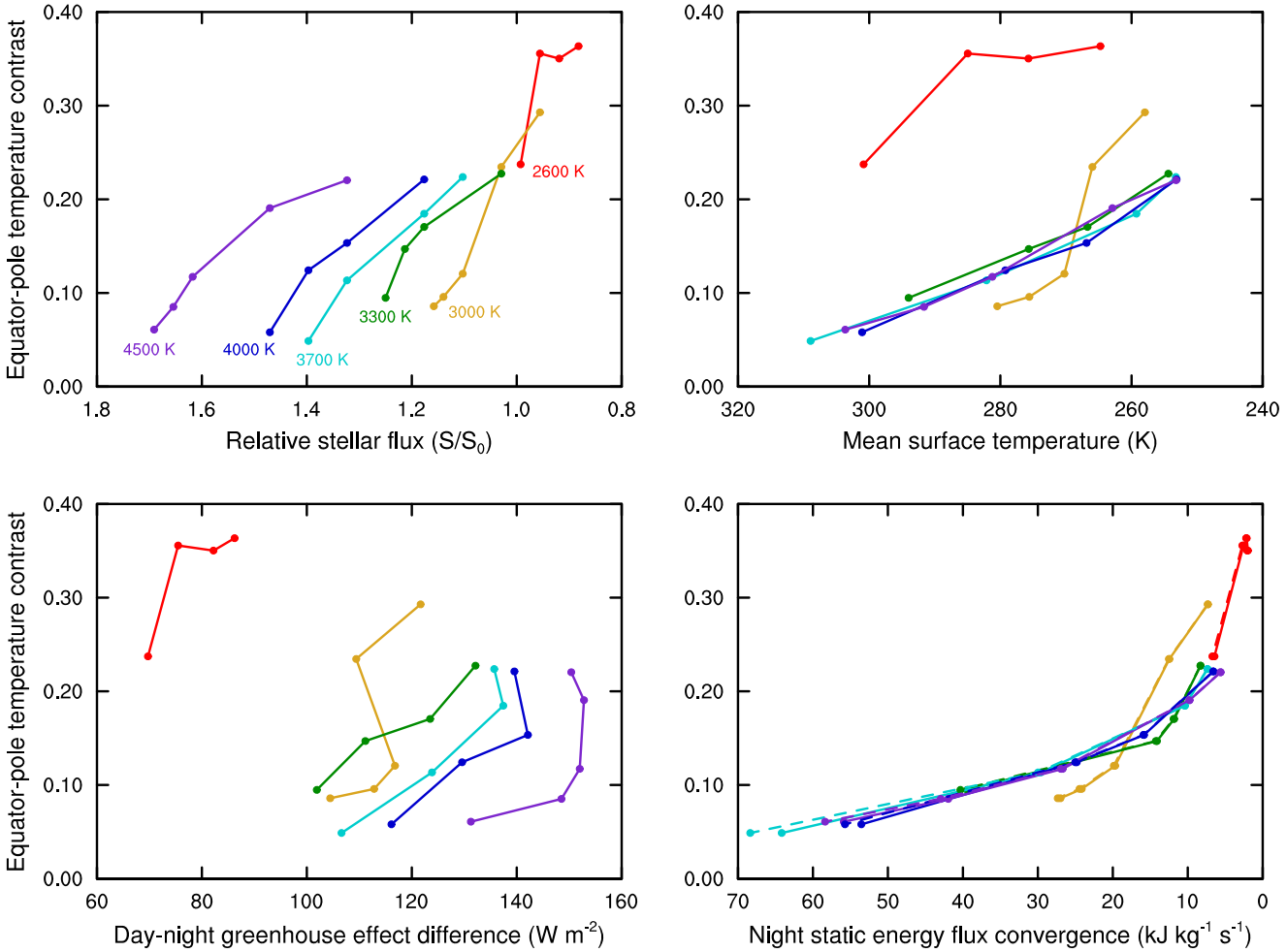

Figure 8. Full set of simulations shown as the scaled equator-to-pole temperature contrast, $(T_{\rm equator}-T_{\rm pole})/T_{\rm eq}$, vs. relative stellar flux, S/S_0, with warmer stars on the left side of the panel (top left). Simulations in the slow rotation regime show a correlation between the scaled equator-to-pole temperature contrast and the mean surface temperature (top right), which corresponds to the decrease in the day–night greenhouse effect difference (bottom left) that occurs in response to the increase in the night-side dry (solid) and moist (dashed) static energy flux convergence (bottom right). The 2600 K rapid rotation and 3000 K Rhines rotation cases show notably different behaviors, due in part to their warmer poles compared to slow rotators.

velocity of the zonal wind less than the gravity wave speed (implying that the Rhines length is smaller than the Rossby deformation radius). Hot atmospheres, such as closely orbiting hot Jupiters, could conceivably host supersonic winds that may fall within this regime. However, this fourth regime is probably not feasible within the terrestrial planet habitable zone.

5. Implications for Observations

All of our simulations show a strong correlation between the day–night surface temperature contrast and the global mean surface temperature, which is driven by the increase in dry static energy flux convergence on the night side (Figure 2). This decrease in day–night contrast can also be interpreted as an increase in the atmospheric optical thickness (Equations (3) and (4)), which suggests that synchronously rotating planets observed near the inner edge of the habitable zone should show a smaller day–night temperature contrast than planets orbiting farther outward. Planets near the outer edge of the habitable zone should build up a dense carbon dioxide atmosphere (Kasting et al. 1993), which also increases the longwave optical depth and thus should decrease the day–night temperature contrast. Observations of the day–night temperature contrast on terrestrial synchronous rotators will provide important constraints on modeling the atmospheres of these planets.

The dynamical regime depends upon the Rossby deformation radius and Rhines length. Planetary rotation period can be inferred from observations of the orbital period for planets around low-mass stars where tidal locking is expected, but the combination of models and observations will be needed to estimate values of the mean wind speed, buoyancy, or other indicators of the Rossby deformation radius and Rhines length. If we assume a fixed Earth-like radius, as with our set of simulations, then we can use the fact that the rotation period is also a function of spectral stellar type (Equation (1)), which allows us to predict the dynamical state of planets in the habitable zone of a given low-mass star. Planets around M-dwarf stars with effective temperatures of 3700–4500 K (rotation period >20 days) should be slow rotators, with thermally direct large-scale circulation from the day to the night side. Other planets around the lowest mass stars we consider, with effective temperatures of less than 3000 K (rotation period <5), should be rapid rotators that exhibit strong upper-level jets with asymmetric flow in the lower troposphere. Stars with effective temperatures in the range of 3000–3300 K (rotation period ∼5–20) represent the intermediate state of Rhines

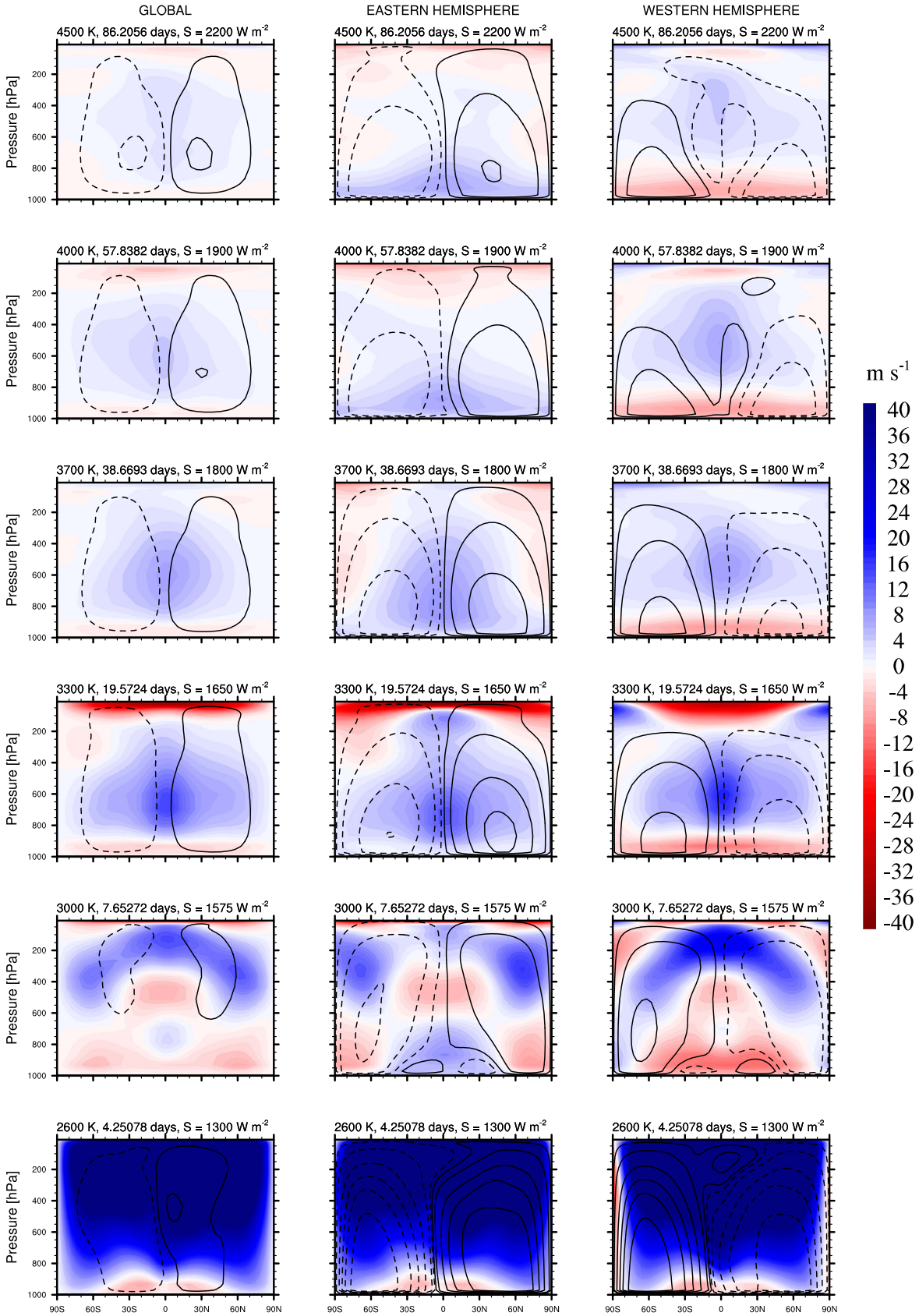

Figure 9. Mean meridional circulation (line contours) and zonal mean zonal wind (shading) averaged across the entire planet (first column), eastern hemisphere (second column), and western hemisphere (third column) from the substellar point. Note that all simulations show circulation patterns in the opposite direction when comparing hemispheres. Contours are drawn at an interval of $\pm\{20, 100, 300, 500, 700, 1000\} \times 10^9$ kg s^{-1}. The solid contours indicate clockwise circulation, and the dashed contours indicate counterclockwise circulation.

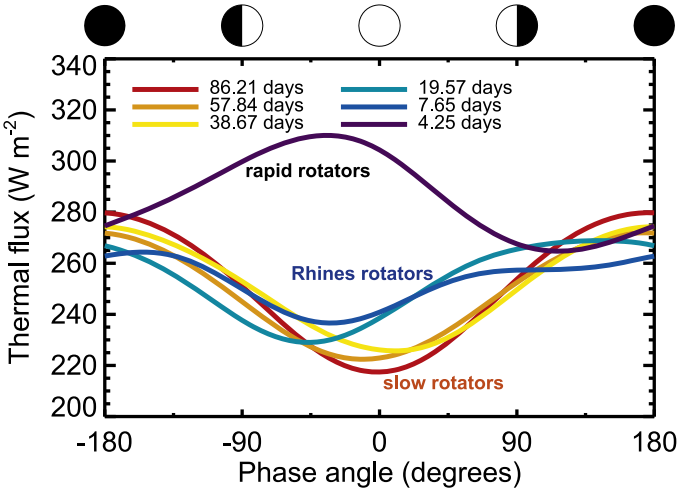

Figure 10. Thermal phase curves can identify synchronously rotating habitable zone planets as slow rotators (minimum thermal flux near 0°), Rhines rotators (minimum thermal flux near −45°), and rapid rotators (maximum thermal flux near −45°).

rotators, which exhibit planetary-scale turbulent flow while still retaining a thermally direct circulation from the day to the night side.

We can apply our model results to think about the expected dynamical regime for recently discovered terrestrial-sized exoplanets, assuming synchronous rotation. The TRAPPIST-1 systems may contain several planets within the traditional liquid water habitable zone, with TRAPPIST-1e being the most promising candidate (Turbet et al. 2017; Wolf 2017). With an orbital period of ∼6 days, TRAPPIST-1e would be close to the rapid rotator regime—especially if its lower planetary mass implies a lower atmospheric scale height (and thus a smaller value of λ_R). Proxima Centauri b has an orbital period of ∼11 days, which places it within the Rhines rotation regime if it is able to sustain an atmosphere. The planet LHS 1140b has a slower rotation period of ∼24 days, which implies that its surface flow and heating should exhibit the near symmetry of the slow rotation regime. These conclusions not only assume that these planets are in synchronous rotation but also that the atmospheric dynamics can be approximated by our 1 bar atmosphere simulations with an Earth-sized planet.

These dynamical regimes can also be extended to planets with a larger radius than Earth. A larger planet has a faster rotation about its axis compared to a smaller planet with equal angular velocity. For example, a planet with Earth-like terrestrial features but a radius twice as large as Earth would be a slow rotator with rotation period less than 10 days and a Rhines rotator with rotation period from ∼10 to 40 days. We also note that changes in atmospheric thickness and composition could also affect the Rossby deformation radius and Rhines number, and therefore the characterization of the atmosphere's dynamical state. Further GCM studies that explore the mass and radius dependence of these dynamical regimes will place better constraints on known and future synchronously rotating exoplanets.

Thermal phase curves have been proposed as a relatively simple method for observing and characterizing terrestrial extrasolar planets (e.g., Cowan et al. 2012). Thermal phase curves show the disk-integrated thermal flux emitted by a planet as seen by the observer as a function of the planet's position in its orbit around the host star. Assuming an (approximately) edge-on orientation, a phase angle of ±180° corresponds to a transit event when only the night side of the planet is in the field of view of the observer. A phase of angle of 0° corresponds with the secondary eclipse, where only the day side of the planet is visible to the observer (excluding the actual secondary eclipse event of course). *JWST* will observe across most infrared wavelengths and may be able to resolve the shape of thermal phase curves for terrestrial planets in nearby M-dwarf systems (Meadows et al. 2016).

We calculate broadband thermal emission phase curves following the method of Koll & Abbot (2015), using outgoing thermal flux maps produced by our GCM simulations, time-averaged over many orbits. In Figure 10, we show the thermal phase curves for six different simulations. Note that the simulations shown in Figure 10 are the same set as shown in Figures 5, 7, and 9. Each of the three dynamical regimes is clearly evident and differentiable within the broadband thermal emission phase curves. The differences between the thermal phase curves for the rapid, slow, and Rhines rotators are a result of the interaction of atmospheric dynamics with clouds and water vapor, which in turn feed back on both the planetary surface temperature and the allowed outgoing thermal radiation at the top of the atmosphere.

For each case, the modulation of the upwelling longwave flux (and thus the thermal emission phase curve) is tied closely to the location of high-altitude water ice (i.e., cirrus) clouds (Figure 11). Cirrus clouds are efficient absorbers of longwave radiation emitted by the planet surface (Ramanathan et al. 1989). Figure 11 shows the water ice cloud condensate mass mixing ratio, specific humidity, upwelling longwave flux, and upwelling longwave clear-sky flux for each dynamical regime, with all atmospheric columns located along the equator. Note that the substellar point is at a longitude of 0°, and the antistellar point is at a longitude of ±180°. The bottom panel of Figure 11 shows that if we omit clouds from the radiative transfer calculation, then the upwelling longwave clear-sky flux is generally uniform. This indicates that cirrus clouds, rather than the advection of water vapor and its associated greenhouse effect, are responsible for the morphology of the thermal phase curves.

Unsurprisingly, for all cases studied, the hottest planetary surface temperatures are found on the day side (Figure 7). In the absence of an atmosphere, or when the greenhouse effect is

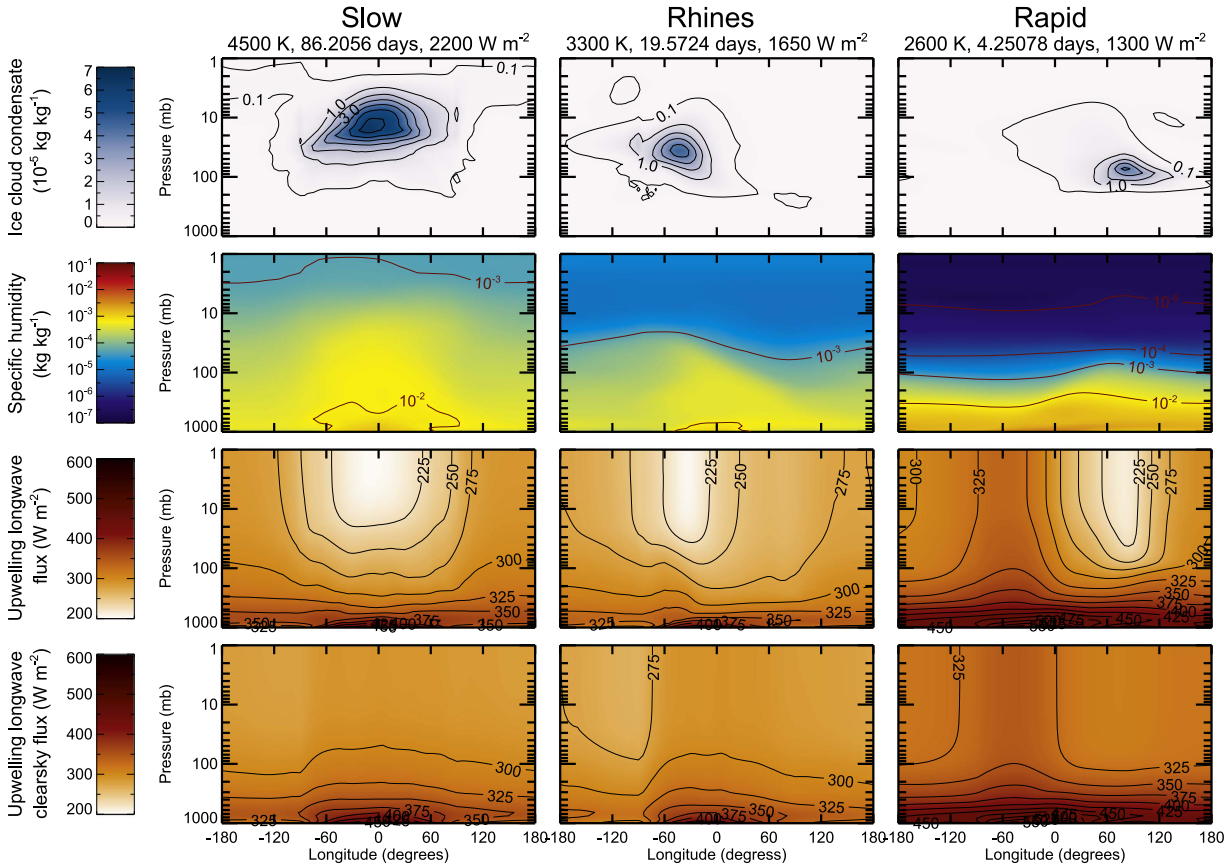

Figure 11. Vertical profiles taken along the equator for ice cloud condensate mass mixing ratio (top row), specific humidity (second row), upwelling longwave flux (third row), and upwelling longwave clear-sky flux (bottom row). The substellar point is located at 0° longitude. Ice clouds form in regions of high specific humidity and cold temperatures, typically above 100 mb. The minimum in upwelling longwave flux corresponds to the maximum in ice cloud condensate for all simulations, because ice clouds are efficient greenhouse absorbers. Slow rotators show areas of high specific humidity and cirrus clouds located immediately over the substellar point. Water vapor, ice clouds, and the associated minima in the outgoing longwave flux are shifted westward of the substellar point for Rhines rotators and eastward of the substellar point for rapid rotators. When clouds are ignored in the radiative transfer calculation, the upwelling longwave clear-sky flux appears generally uniform across all longitudes.

perfectly uniform everywhere, the thermal emission phase curve should mirror the disk-integrated surface temperature distribution as a function of phase angle. However, cirrus clouds ultimately control where thermal energy can be effectively emitted to space. Rapid rotators exhibit a maximum in thermal emission when viewing the day side of the planet. Clouds on rapid rotating worlds are advected eastward off of the substellar point by the strongly superrotating atmosphere. A minimum in the thermal emission is coincident with the primary cirrus cloud deck that is located near the eastern terminator of the planet (Figure 11). Locations immediately west of the substellar point have relatively few clouds (e.g., Kopparapu et al. (2017) Figure 8), resulting in both warmer surface temperatures and efficient emission of thermal energy to space. Thus, the maximum in the thermal phase curve for rapid rotators is shifted ∼45° west of the substellar point (Figure 10), where surface temperatures are warm and clouds are absent.

For slow rotators again, the surface temperature maximum is found at the substellar point; however, thick and symmetric clouds completely enshroud the day-side hemisphere. A thick cap of high-altitude cirrus clouds significantly reduces the outgoing thermal flux from the day side by lowering the emitting temperature of the atmosphere (Figure 11). The night side remains cloud free and can efficiently radiative energy to space. The night-side thermal emission remains large despite cold surface temperatures, due to the near-surface inversion layer described in Section 3 and the low water vapor concentration, which allows the night side to act as a "radiator fin" that emits excess thermal energy to space similar to the dry subtropics of Earth (Yang & Abbot 2014). This results in a minimum in the thermal phase curve when viewing the day side of the planet and in a maximum when viewing the night side for slow rotators, as first noted by Yang et al. (2013). Note that the thermal phase curve for slow rotators exhibits remarkable symmetry with minima at 0° and maxima at ±180°, due to the symmetric day–night general circulation that occurs on these worlds. We also note that ocean heat transport will affect these results, as surface fluxes induced by the ocean can be significant and can also depend upon the planetary rotation period (Cullum et al. 2014; Hu & Yang 2014; Way et al. 2015), although the presence of continents could limit the magnitude of ocean heat transport (Yang et al. 2013).

While differences between fast and slow rotators are evidently clear, the differentiation of Rhines rotators is more subtle. The thermal phase curve for Rhines rotators is qualitatively similar to that of slow rotators; however, the minimum is shifted ∼45° westward of the substellar point. Tropospheric water clouds still generally permeate the substellar hemisphere of Rhines rotators, keeping albedos large and suppressing the surface temperature. However, the primary ice cloud layer is shifted westward of the substellar point,

shifting the associated minimum in the thermal phase curve accordingly. This corresponds to the strong westerly jet present in the uppermost model layers of this Rhines rotator (Figure 9, middle row), which is nonexistent in the slow rotators and extremely weak in the rapid rotators. Rhines rotators may be differentiated from slow rotators by the offset of the minimum in the thermal phase curve. Our results imply that understanding the stratospheric process and ice cloud formation on terrestrial extrasolar planets may be critical for interpreting the observed thermal phase curves, although we caution that further studies with other GCMs, using different ice cloud parameterizations, will be needed to demonstrate the robustness of these phase curve features.

6. Conclusion

Our examination of the atmospheres of planets in synchronous rotation around low-mass stars reveals three distinct dynamical regimes (Figure 4). Rapid rotation occurs when the Rossby deformation radius is less than the planetary radius (rotation period >5 days). Slow rotation occurs when both the Rossby deformation radius and the Rhines length are greater than the planetary radius (rotation period >20 days). Rhines rotation occurs when the Rhines length is less than the planetary radius but the Rossby deformation radius is greater than the planetary radius, which allows turbulent structures to reach planetary scales (rotation period $\sim$5–20 days).

These three dynamical states can be distinguished from one another through observations of the thermal phase curve of the planet. Differences in the amplitude of the maxima and minima of the thermal phase curves can be used to identify the slow rotation regime, while the transition between the rapid rotation and Rhines regimes can be identified by comparing the morphology of the thermal phase curves. Corroborating these phase curves with observations of the planet's orbital period and the host star's spectral type will provide a basis for further characterization of such atmospheres with computational models.

We also show that the day–night surface temperature contrast for terrestrial planets decreases as incident stellar flux increases. The combined effects of moisture accumulation and the increase in static energy flux divergence on the night side leads to an increase in the greenhouse effect, which diminishes the temperature contrast between the day and night sides. We therefore expect that synchronously rotating planets near the inner edge of the habitable zone should have diminished the day–night surface temperature contrasts compared with other synchronous rotators at farther orbital distances.

We can apply these results to the response of a synchronously rotating atmosphere under the steady main-sequence brightening of its host star. Planets in the slow rotation regime respond to an increase in stellar forcing with a decrease in both the day–night temperature contrast and the root mean squared surface wind, whereas planets in the Rhines and slow rotation regimes respond to a similar increase by decreasing the day–night to equator–pole temperature contrast ratio. This suggests that the atmospheres of slow rotators will adapt by reducing the equatorial day–night temperature contrast with an increase in the static energy flux convergence on the night side. Rhines and slow rotators will react by increasing the equator–pole contrast more than the day–night contrast, tending toward a surface temperature distribution with even heating at all latitudinal bands. It is beyond the scope of this paper to speculate as to which of these three regimes, if any, would be conducive or adverse to the presence of life. But we can at least begin to think about how the evolution of a low-mass star can affect the dynamical state of a planet within its habitable zone.

The authors thank Jun Yang for constructive comments that greatly improved the manuscript. J.H., E.T.W., and R.K.K. acknowledge funding from the NASA Habitable Worlds program under award NNX16AB61G. R.K.K. also acknowledges funding from NASA Astrobiology Institute's Virtual Planetary Laboratory lead team, supported by NASA under cooperative agreement NNH05ZDA001C. X.Z. acknowledges support from NSF grant AST1740921. This work was facilitated through the use of advanced computational, storage, and networking infrastructure provided by the Hyak supercomputer system at the University of Washington. This work benefited from the Exoplanet Summer Program in the Other Worlds Laboratory (OWL) at the University of California, Santa Cruz, a program funded by the Heising-Simons Foundation. Any opinions, findings, and conclusions or recommendations expressed in this material are those of the authors and do not necessarily reflect the views of NASA or NSF.

Appendix
Static Energy Flux Convergence by Isallobaric Wind

As stellar flux increases, slow rotators and Rhines rotators show a decrease in day–night temperature contrast that corresponds with an increase in the night- (day-) side static energy flux convergence (divergence). We demonstrate here that this relationship is ultimately driven by an increase in the night- (day-) side convergence (divergence) of the component of wind driven by pressure contrasts known as the isallobaric wind.

Let $\boldsymbol{v}$ be the horizontal wind vector and $s = c_p T + \Phi + L_v q$ be the moist static energy per unit mass. The static energy flux divergence can be written as

$$\nabla \cdot (\boldsymbol{v}s) = s\nabla \cdot \boldsymbol{v} + \boldsymbol{v} \cdot \nabla s, \tag{10}$$

where the first term on the right is the horizontal wind divergence, and the second term on the right is the advection of static energy. Static energy *divergence* refers specifically to the situation when $\nabla \cdot (\boldsymbol{v}s) > 0$, while static energy *convergence* implies that $\nabla \cdot (\boldsymbol{v}s) < 0$. We are primarily concerned with comparing $\nabla \cdot (\boldsymbol{v}s)$ between the day and night sides, where the day side is characterized by heating across much of the hemisphere and the night side is characterized by near-uniform cold temperatures across most of the hemisphere. This suggests that we can simplify Equation (10) by assuming $\nabla s \approx 0$ for these atmospheres.

The geostrophic wind describes the balance between the pressure gradient force and Coriolis force, which we can write as

$$\boldsymbol{v}_g = \boldsymbol{k} \times \frac{1}{\rho f} \nabla p, \tag{11}$$

where $\boldsymbol{k}$ is the upward unit vector, f is the Coriolis parameter, ρ is the air density, and p is the pressure. However, we cannot substitute $\boldsymbol{v}_g$ for $\boldsymbol{v}$ in Equation (10) because the geostrophic wind is non-divergent ($\nabla \cdot \boldsymbol{v}_g = 0$). We instead consider the quasi-geostrophic approximation, where the wind vector is the sum of geostrophic and ageostrophic components, $\boldsymbol{v} = \boldsymbol{v}_g + \boldsymbol{v}_a$.

The quasi-geostrophic approximation allows us to express the ageostrophic wind as

$$\begin{aligned} \boldsymbol{v}_a &= \frac{1}{f}\boldsymbol{k} \times \frac{D\boldsymbol{v}_g}{Dt} \\ &= \frac{1}{f}\boldsymbol{k} \times \frac{\partial \boldsymbol{v}_g}{\partial t} + \frac{1}{f}\boldsymbol{k} \times (\boldsymbol{v}_g \cdot \nabla \boldsymbol{v}_g). \end{aligned} \tag{12}$$

The two terms on the bottom line of Equation (12) respectively represent the isallobaric and advective components of the ageostrophic wind. The advective term can contribute to ageostrophic wind divergence through positive vorticity advection; however, vorticity advection between the day and night hemispheres is small. We therefore focus our analysis on the contribution of the isallobaric wind to the static energy flux.

The isallobaric wind is perpendicular to lines of constant geopotential tendency (known as isallobars) and describes the flow toward regions of falling pressure. Substituting from Equation (11), we write the isallobaric wind, $\boldsymbol{v}_{\rm is}$, as

$$\boldsymbol{v}_{\rm is} = \frac{-1}{f^2 \rho} \nabla \left(\frac{\partial p}{\partial t} \right). \tag{13}$$

We now replace the total wind vector in Equation (10) with the isallobaric wind in Equation (13) to obtain

$$\nabla \cdot (\boldsymbol{v}s) \approx s \nabla \cdot \boldsymbol{v}_{\rm is} = \frac{-s}{f^2 \rho} \nabla^2 \left(\frac{\partial p}{\partial t} \right). \tag{14}$$

Equation (14) shows that an increase (decrease) in pressure corresponds to a divergence (convergence) of the isallobaric wind. For synchronous rotators, the increase in pressure due to fixed stellar heating on a single hemisphere causes the isallobaric wind, as well as the static energy flux, to diverge on the day side and converge on the night side, which decreases the day–night temperature contrast.

ORCID iDs

Jacob Haqq-Misra https://orcid.org/0000-0003-4346-2611
Eric. T. Wolf https://orcid.org/0000-0002-7188-1648

References

Allard, F., Allard, N. F., Homeier, D., et al. 2007, A&A, 474, L21
Anglada-Escudé, G., Amado, P. J., Barnes, J., et al. 2017, Natur, 536, 437
Bintanja, R., Graversen, R. G., & Hazeleger, W. 2011, NatGe, 4, 758
Carone, L., Keppens, R., & Decin, L. 2014, MNRAS, 445, 930
Carone, L., Keppens, R., & Decin, L. 2015, MNRAS, 452, 2413
Carone, L., Keppens, R., & Decin, L. 2016, MNRAS, 461, 1981
Cowan, N. B., Voigt, A., & Abbot, S. 2012, ApJ, 757, 80
Cullum, J., Stevens, D., & Joshi, M. 2014, AsBio, 14, 645
Curry, J. A., Schramm, J. L., Rossow, W. B., & Randall, D. 1996, JCli, 9, 1731
Dole, S. H. 1964, Habitable Planets for Man (New York: Blaisdell)
Edson, A., Lee, S., Bannon, P., Kasting, J. F., & Pollard, D. 2011, Icar, 212, 1
Fujii, Y., Del Genio, A. D., & Amundsen, D. S. 2017, ApJ, 848, 100
Geisler, J. E. 1981, JAtS, 38, 1390
Gill, A. 1982, InGeo, 30, 436
Gillon, M., Triaud, A. H., Demory, B. O., et al. 2017, Natur, 542, 456
Haberle, R. M., McKay, C. P., Tyler, D., & Reynolds, R. T. 1996, in Circumstellar Habitable Zones, ed. L. R. Doyle (Menlo Park, CA: Travis House), 29
Haqq-Misra, J., & Kopparapu, R. K. 2015, MNRAS, 446, 428
Hu, Y., & Yang, J. 2014, PNAS, 111, 629
Joshi, M. M. 2003, AsBio, 3, 415
Joshi, M. M., Haberle, R. M., & Reynolds, R. T. 1997, Icar, 129, 450
Kasting, J. F., Whitmire, D. P., & Reynolds, R. T. 1993, Icar, 101, 108
Koll, D. D. B., & Abbot, D. S. 2015, ApJ, 802, 21
Koll, D. D. B., & Abbot, D. S. 2016, ApJ, 825, 99
Komacek, T. D., & Showman, A. P. 2016, ApJ, 82, 16
Komacek, T. D., Showman, A. P., & Tan, X. 2017, ApJ, 835, 198
Kopparapu, R. K., Ramirez, R., Kasting, J. F., et al. 2013, ApJ, 765, 131
Kopparapu, R. K., Ramirez, R., SchottelKotte, J., et al. 2014, ApJL, 787, L29
Kopparapu, R. K., Wolf, E. T., Arney, G., et al. 2017, ApJ, 845, 5
Kopparapu, R. K., Wolf, E. T., Haqq-Misra, J., et al. 2016, ApJ, 819, 1
Leconte, J., Forget, F., Charnay, B., et al. 2013, A&A, 554, A69
Liu, Y., Key, J. R., Schweiger, A., & Francis, J. 2006, JCli, 19, 4902
Meadows, V. S., Arney, G. N., Schwieterman, E., et al. 2016, arXiv:1608.08620
Merlis, T., & Schneider, T. 2010, JAMES, 2, 13
Noda, S., Ishiwatari, M., Nakajima, K., et al. 2017, Icar, 282, 1
Perez-Becker, D., & Showman, A. P. 2013, ApJ, 776, 134
Ramanathan, V., Cess, R. D., Harrison, E. F., et al. 1989, Sci, 243, 57
Rhines, P. B. 1975, JFM, 69, 417
Selsis, F., Kasting, J. F., Levrard, B., et al. 2007, A&A, 476, 1373
Selsis, F., Wordsworth, R. D., & Forget, F. 2011, A&A, 532, A1
Showman, A. P., Cho, J. Y.-K., & Menou, K. 2010, in Exoplanets, ed. S. Seager (Tucson, AZ: Univ. Arizona Press), 471
Showman, A. P., & Guillot, T. 2002, A&A, 385, 166
Showman, A. P., Wordsworth, R. D., Merlis, T. M., & Kaspi, Y. 2013, in Comparative Climatology of Terrestrial Planets, ed. S. J. Mackwell et al. (Tucson, AZ: Univ. Arizona Press), 277
Turbet, M., Bolmont, E., Leconte, J., et al. 2017, A&A, in review
Vallis, G. K. 2017, Atmospheric and Oceanic Fluid Dynamics: Fundamentals and Large-Scale Circulation (2nd ed.; Cambridge: Cambridge Univ. Press)
Way, M. J., Del Genio, A. D., Kelley, M., et al. 2015, arXiv:1511.07283
Wolf, E. T. 2017, ApJL, 839, L1
Wordsworth, R. 2015, ApJ, 806, 180
Yang, J., & Abbot, D. S. 2014, ApJ, 784, 155
Yang, J., Boué, G., Fabrycky, D. C., & Abbot, D. S. 2014, ApJL, 787, L2
Yang, J., Cowan, N. B., & Abbot, D. S. 2013, ApJL, 771, L45
Zhang, X., & Showman, A. P. 2017, ApJ, 836, 73